Giant anomalous Nernst effect in the Co_{2}MnAl_{1−x}Si_{x} Heusler alloy induced by Fermi level tuning and atomic ordering

Y. Sakuraba, K. Hyodo, A. Sakuma, and S. Mitani

Phys. Rev. B **101**, 134407 — Published 6 April 2020

DOI: 10.1103/PhysRevB.101.134407

Fermi level tuning and atomic ordering induced giant anomalous Nernst effect in $Co_2MnAl_{1-x}Si_x$ Heusler alloy

Y. Sakuraba[1,2], K. Hyodo[3], A. Sakuma[3] and S. Mitani[1]

[1]Research Center for Magnetic and Spintronic Materials, National Institute for Materials Science, Sengen 1-2-1, Tsukuba, Ibaraki, 305-0047 Japan

[2] PRESTO, Japan Science and technology Agency, Saitama 332-0012, Japan

[3] Department of Applied Physics, Tohoku University, Aoba-ku, Sendai, 980-8579, Japan

Abstract

Co_2MnAl has been predicted to have Weyl points near Fermi level which is expected to give rise to exotic transverse transport properties such as large anomalous Hall(AHE) and Nernst effects(ANE) due to large Berry curvature. In this study, the effect of Fermi level position and atomic ordering on AHE and ANE in $Co_2MnAl_{1-x}Si_x$ were studied systematically. The Co_2MnAl film keeps *B*2-disordred structure regardless of annealing temperature, which results in much smaller anomalous Hall conductivity σ_{xy} and transverse Peltier coefficient α_{xy} than those calculated for $L2_1$-ordered Co_2MnAl. Our newly performed calculation of σ_{xy} with taking *B*2 disordering into account well reproduces experimental result, thus it was concluded that Berry curvature originating from Weyl points is largely reduced by *B*2 disordering. It was also revealed Al substitution with Si shifts the position of Fermi level and improves the $L2_1$-atomic ordering largely, leading to strong enhancement of α_{xy}, which also agreed with our theoretical calculation. The highest thermopower of ANE of 5.7μV/K, which is comparable to the recent reports for Co_2MnGa, was observed for $Co_2MnAl_{0.63}Si_{0.37}$ because of dominant contribution of α_{xy}. This study clearly shows the importance of both Fermi level tuning and high atomic ordering for obtaining the effect of topological feature in Co-based Heusler alloys on transverse transport properties.

Anomalous Nernst effect (ANE), which is a thermoelectric phenomenon unique to magnetic materials, has attracted attention because of several unique advantages for thermoelectric applicatioins.[1–3] Here, the electric field of ANE ($\vec{E}_{ANE}$) can be expressed by the following equation,

$$\vec{E}_{ANE} = Q_S\left(\mu_0\vec{M} \times \nabla T\right) \ , \qquad (1)$$

where Q_S and $\mu_0\vec{M}$ represent the anomalous Nernst coefficient and magnetization, respectively. As equation (1) indicates, ANE generates an electric field in the direction of the outer product of the magnetization $\mu_0\vec{M}$ and temperature gradient ∇T. This three dimensionality of ANE enables us to increase the serial voltage by using thermopiles consisting of simple laterally connected magnetic wires, because $\vec{E}_{ANE}$ appears along the surface of a heat source. This is a significant advantage for enlarging the size of the TEG module and utilizing large-area of non-flat heat sources. In addition to such attractive feature for practical applications, recent finding of large ANE originating from the materials having topological features such as Mn_3Sn[4] stimulated studies on ANE for gaining a fundamental understanding of the phenomenon and enhancing its thermopower.[3-17] It has been recently reported that, ferromagnetic Heusler alloy Co_2MnGa showed the largest thermopower of ANE of about 6 μV/K[7,8], which is one order of magnitude larger than that the conventional ferromagnets in Fe, Co and Ni.[18] Such large thermopower was explained as an exotic property of a magnetic Weyl semimetal in Co_2MnGa. Namely, large transverse thermoelectric effect intrinsically appears in Co_2MnGa due to its large Berry curvature near Fermi level (E_F)

because of the formation of Weyl points on the nodal lines of electronic bands by the spin-orbit interaction[6,8,9]. Such a topological feature of magnetic material has attracted worldwide interest for not only fundamental physics but also its great potential of practical applications. One curious issue yet to be clarified in Heusler alloy-based Weyl semi-metals is how the atomic ordering and the position of E_F against the Weyl points affect the sign and magnitude of ANE. Since previous studies for ANE in Heusler alloy-based Weyl semi-metals have focused on the bulk single crystal or epitaxial thin film having high $L2_1$ atomic ordering and the stoichiometric composition[7,8,17], it is still unclear how much ANE is sensitive to the atomic ordering and chemical composition both theoretically and experimentally.

In the present study, we paid attention to Co_2MnAl which is another interesting material predicted to show large intrinsic AHE[19,20] due to the existence of Weyl points near E_F [21]. Previous experiment claimed the observation of large AHE in the Co_2MnAl film having a random disordering of Mn and Al, so called, $B2$ disorder(Fig. 1(a),(b)).[22] However, they showed only anomalous Hall resistivity ρ_{xy} as a evidence of large AHE and did not compare anomalous Hall conductivity σ_{xy} with the theoretical value although σ_{xy} is the intrinsic physical parameter that is theoretically accessible[23,24]. Therefore, strictly speaking, the theoretically predicted large AHE has never been confirmed in Co_2MnAl. It is well known that it is not easy to form $L2_1$-ordering in Co_2MnAl especially in thin film[22,25]. Co_2MnAl often has B2-ordering in which Mn and Al atoms are randomly disordered because of too small driving force to form $L2_1$ as indicated by very low $L2_1$ to B2 order-disorder transition temperature $T_t^{L2_1/B2}$ of

950K[26], which is much lower than $T_t^{L2_1/B2}$ in Co_2MnGa, 1200K. It is expected that the atomic ordering in Co_2MnAl can be largely improved by the replacement of Al with Si because $L2_1$-Co_2MnSi is the thermally stable intermetallic ordered compound that keeps $L2_1$ ordered structure up to its melting temperature ~ 1400K, namely, $T_t^{L2_1/B2}$ was estimated to be 1580K [27],that is higher than its melting point. In addition, previous study revealed that the position of E_F in Co_2MnAl can be tuned toward higher energy by substituting Si with Al.[28,29] Therefore, $Co_2MnAl_{1-x}Si_x$ is a suitable material to investigate how the position of Weyl points against E_F and atomic ordering influences AHE and ANE.

(001)-oriented epitaxial $Co_2MnAl_{1-x}Si_x$ (CMAS) thin films having different Si:Al ratios were grown on a MgO (001) substrate using a co-sputtering technique with Co_2MnSi and Co_2MnAl sputtering targets. All films were deposited at ambient substrate temperature and then in-situ annealed at 600°C. The composition of the films was measured by a combination of inductively coupled plasma mass spectrometry (ICP-MS) and x-ray fluorescence analysis (XRF). In this study we made twelve CMAS thin films having a different Si:Al composition ratio x. The compositions of two CMAS films having nominal x = 0 and 0.25 were measured by ICP-MS and determined to be nearly stoichiometry $Co_{1.93}Mn_{0.98}Al_{1.08}$ and $Co_{1.88}Mn_{0.95}Al_{0.90}Si_{0.27}$ in at.%, respectively. Although we found a slight off-stoichiometry of Co and Mn compositions, we focus on the effect of Si:Al ratio x on various properties in this study. Thus, the x for all CMAS

films is evaluated by XRF to be 0.00, 0.11, 0.14, 0.15, 0.22, 0.23, 0.29, 0.32, 0.37, 0.48, and 1.00. For simplification, we express each CMAS films in "$Co_2MnAl_{1-x}Si_x$" using x measured by XRF. The annealing temperature T_{ann} dependence was studied for the films with x = 0 and 0.37 from 500 to 700°C to investigate the atomic ordering effect on ANE. The thickness of the films was fixed at 30 nm. The crystal structure and atomic ordering were investigated by x-ray diffraction with a Cu K_α source. Longitudinal and transverse electric and thermoelectric transport properties including ANE were investigated with a physical property measurement system (PPMS) for films patterned by photolithography and Ar ion milling. The electric resistivity ρ_{xx} was measured using a dc four-probe method by flowing a constant dc current of 1 mA. ANE (AHE) was measured by flowing a heat (electric) current in the film plane direction and applying a magnetic field in the perpendicular direction in PPMS at 300K. As for ANE, the temperature gradient ∇T in PPMS was carefully evaluated through the following procedure : First ∇T outside of PPMS was measured using an infrared camera (InfReC R450, Nippon Avionics) for the sample with the black body coating to correct the emissivity of the samples. At the same time, the Seebeck voltage V_{SE} in the film was measured outside, then the linear relationship between V_{SE} and ∇T was obtained. After that, ANE voltage V_{ANE} was measured together with V_{SE} in PPMS, then ∇T in PPMS can be estimated through the V_{SE}. The same technique has been utilized in our previous study.[30] To improve the quantitative reliability of observed ∇T in this study, we measured the given ∇T by the patterned on-chip thermometer, that was employed in ref.17, for one of our samples and gave a calibration to ∇T measured by the method using IR camera

(see the supplemental Material for detail[30]). For a strict evaluation of Seebeck coefficient S_{SE}, we used the Seebeck Coefficient/Electric Resistance Measurement System (ZEM-3, ADVANCE RIKO, Inc.). We also performed a first principles calculation to evaluate σ_{xy}. The first-principles technique was the tight binding-linearized muffin-tin orbital method under the local spin-density approximation[31]. To consider the AHE effect, the spin-orbital-coupling term under the Pauli approximation was added to the non-relativistic Hamiltonian. σ_{xy} was calculated from the Kubo-Bastin formula consisting of Fermi-surface and –sea terms[32]. Since previous theoretical studies have calculated σ_{xy} in only ideal $L2_1$-ordered cases[19,20], in this study the electron scattering effect originating from $B2$ disorder on σ_{xy} was taken into account in the coherent-potential-approximation[31] with our own developed scheme of the calculation[33]. About 5×10^7 $\boldsymbol{k}$-points were used for the Fermi-surface term and from 1×10^6 to 5×10^7 depending on the energy variable in the integration for the Fermi-sea term in the full Brillouin zone [32]. ,

Out-of-plane XRD patterns for the CMAS films annealed at 600°C are shown in Figure 1(c). We clearly detected only (002) and (004) peaks from all CMAS films, indicating (001)-oriented growth in the whole range of x. A clear (002) super lattice peak indicates the existence of atomic ordering between Co and (Mn,Al/Si) sites so-called $B2$ structure (Fig.1(b)). The out-of-plane lattice constant a, as evaluated from the (004) peak position, is plotted against x in the inset of Fig. 1(c). The a for Co_2MnAl and Co_2MnSi films are 5.74 and 5.63 Å, respectively, which is similar with the reported

values in literature, 5.755 and 5.654 Å.[27] The a almost linearly decreases with increasing Si composition ratio, following Vegard's law, indicating a formation of single phase CMAS in whole range of x. We also measured the (111) super lattice peak arising $L2_1$-ordered structure by tilting the film plane to 54.7° from the normal direction. No (111) peak appears from x = 0 to 0.15, but tiny detectable peak is observed from x = 0.22 to 0.48 as shown in Figure1(d). The (111) peak intensity appears to be larger with increasing Si composition ratio and the strongest peak was observed in Co_2MnSi, which can be explained by enlargement of $T_t^{L21/B2}$ by the substitution of Si with Al in Co_2MnAl as mentioned earlier. For evaluating the degree of $B2$ and $L2_1$-ordering, S_{B2} and S_{L21}, we performed the XRD pattern simulation for $L2_1$-ordered Co_2MnAl and Co_2MnSi using Visualization for Electronic and Structural Analysis (VESTA) and then calculated S_{B2} and S_{L21} using the following equations.

$$S_{B2}^2 = \frac{I_{002}^{obs}/I_{004}^{obs}}{I_{002}^{sim}/I_{004}^{sim}} \qquad (2)$$

$$S_{L21}^2 = \frac{I_{111}^{obs}/I_{004}^{obs}}{I_{111}^{sim}/I_{004}^{sim}} \qquad (3)$$

Here I_{hkl}^{sim} is the simulated (hkl) peak intensity after giving a correction by considering the multiplicity factor, absorption factor and Lorentz-polarization factor. I_{hkl}^{obs} is the integrated peak intensity for experimentally observed (hkl) peak. The x dependence of $I_{002}^{obs}/I_{004}^{obs}$, $I_{111}^{obs}/I_{004}^{obs}$, S_{B2} and S_{L21} are summarized in Fig.1(e) and (f). We confirmed that degree of S_{B2} is nearly 1 in the whole range of x, indicating nearly perfect B2-ordering exists in these CMAS films. In contrast, S_{L21} is much smaller than 1; S_{L21} =

0 from x = 0 to 0.15, 0.32-0.37 from x = 0.22 to 0.48, and 0.57 for x = 1. This imperfection of $L2_1$-ordering affects the AHE and ANE as discussed later.

Recent study clearly found that the sign of AMR in Co-based Heusler is sensitive to the position of E_F inside/outside the energy gap in minority spin channel(half-metalic gap), namely, the sign of AMR is negative(positive) when E_F is inside(outside) of half-metallic gap.[29,34,35] Therefore we measured AMR for our CMAS films to see the change of E_F position indirectly and found the clear sign change from positive to negative from CMA to CMS at around x = 0.4.(see Supplemental Material[35]). This result supports the E_F shifting toward higher energy by replacing Si with Al as we expected.

Figure 2(a) shows the perpendicular magnetic field dependence of the anomalous Hall resistivity ρ_{yx} for the CMAS thin films measured at 300 K. The Co_2MnAl film had the largest ρ_{yx} of about +18 μΩ·cm which is very close value with the previous study[22]. ρ_{yx} almost monotonically decreases upon replacing Al with Si, as shown in Figure 2(b), and the Co_2MnSi film had the smallest ρ_{yx}, 0.7 μΩ·cm. This result well agrees with the previous study of Hall effect in $Co_2MnSi_{1-x}Al_x$ polycrystalline bulk samples reported by Prestigiacomo et al.[36] The longitudinal conductivity ρ_{xx} shown in Fig.2(b) is nearly constant of about 240-260 μΩcm in the region of x = 0 to 0.32 , and then reduces down to 83 μΩcm from 0.37 to 1.00, which must be more or less related with the improvement of $L2_1$-ordering with Si. The anomalous Hall angle θ_{AHE} and anomalous Hall conductivity σ_{xy} are evaluated using the equations$\theta_{AHE} = -\rho_{yx}/\rho_{xx}$

and $\sigma_{xy} = \rho_{yx}/(\rho_{xx}^2 + \rho_{yx}^2)$, respectively, and plotted in Figs.2(d) and (e). θ_{AHE} clearly monotonically decreases with increasing Si; Co_2MnAl showed the largest magnitude of anomalous Hall angle, $|\theta_{AHE}|$ of 7.3%, whereas $|\theta_{AHE}|$ decreases with x to 0.8% in Co_2MnSi. It should be noted here that the σ_{xy} obtained for Co_2MnAl and Co_2MnSi are 295(362) and 96(101) S/cm at 300K(10K), respectively, which are lower than the calculated intrinsic contribution of AHE, σ_{xy}^{int}, 1265 and 193 S/cm for $L2_1$-ordered Co_2MnAl and Co_2MnSi[20]. Since the theoretical intrinsic mechanism contribution for AHE does not take any electron scattering effect into consideration, experimentally observed σ_{xy} in thin films is reduced even at low temperature by unavoidable scatterings at the surface/interface such as the film surface, film/substrate interface, and grain boundaries. As the σ_{xy} in Fe epitaxial film reduces with decreasing its thickness[37], the existence of electron scattering can be one reason for $\sigma_{xy} < \sigma_{xy}^{int}$. However, the deviation between σ_{xy} and σ_{xy}^{int} for Co_2MnAl seems too large (see Figure 2(e)) to be explained by such an additional scattering. To understand this mechanism, we calculated density of state (DOS) and σ_{xy}^{int} for no only $L2_1$ and but also $B2$ Co_2MnAl . As shown in Fig.3(c), calculated σ_{xy}^{int} in $L2_1$-Co_2MnAl exhibits large variation from 300 to 1600S/cm within even small $\pm$ 0.3eV range around E_F and takes large value of 931S/cm at E_F. On the other hand, disordered $B2$-Co_2MnAl was predicted to show much smaller σ_{xy}^{int}, 258S/cm, at E_F with small slope against energy. As shown in Fig.2(e), this σ_{xy}^{int} for B2-Co_2MnAl is close to the experimental σ_{xy}. Although it has not been elucidated by our calculation that how Berry curvature in the momentum space changes from $L2_1$ to $B2$ disordering structures, it is expected the $B2$ disorder

207 smears the whole band dispersion including the bands forming the Weyl points, which
208 must reduce the Berry curvature near Fermi level. This smearing effect of band
209 dispersion can be seen from the blurred total DOS of B2 structure compared to the sharp
210 DOS of $L2_1$ as shown in Figs.3(a) and 3(c). Thus, it is concluded that observed small
211 σ_{xy} in B2-Co_2MnAl film is attributed to this intrinsic reduction of σ_{xy}^{int} from $L2_1$ to B2.
212 To see Si substitution effect, we also calculated DOS and σ_{xy}^{int} for $L2_1$ and $B2$
213 $Co_2MnAl_{0.63}Si_{0.37}$ as shown in Figs.3(b) and (d), respectively. If one compares the DOS
214 in $L2_1$-ordered Co_2MnAl and $Co_2MnAl_{0.67}Si_{0.33}$ shown in Figs.3(a) and (b), it is clearly
215 confirmed that the E_F shifts by about +0.2 eV with keeping the shape of DOS near E_F.
216 Because of this shift of E_F, the peak of σ_{xy}^{int} we can see near E_F in $L2_1$-Co_2MnAl
217 appears at around -0.22 eV in $Co_2MnAl_{0.63}Si_{0.37}$. Consequently, we can see small
218 difference of σ_{xy}^{int} between $L2_1$ and $B2$, 370 and 268 S/cm, in $Co_2MnAl_{0.63}Si_{0.37}$, which
219 can be an explanation for observed small σ_{xy} in the $Co_2MnAl_{0.63}Si_{0.37}$ film and other
220 CMAS films of x = 0.22-0.51 regardless of their partial $L2_1$-ordering.
221
222 The x dependence of thermopower of ANE and Seebeck effect (S_{ANE} and S_{SE} ,
223 respectively) are summarized in Figure 4(a) and (b). Interestingly, the Co_2MnAl film
224 that showed the largest AHE exhibits a small S_{ANE} of +0.9 μV/K, and S_{ANE} gradually
225 grows as more Al is substituted with Si. The largest S_{ANE} of +3.6 μV/K was observed
226 for $Co_2MnAl_{0.63}Si_{0.37}$. Above x = 0.37 the S_{ANE} reduces with following x, finally drops
227 down to + 0.7 μV/K for Co_2MnSi. On the other hand, the sign of S_{SE} is negative in the
228 whole range of x. With increasing x, the magnitude of S_{SE} gradually increases with x

from -7.7 μV/K in Co_2MnAl to -21.1 μV/K in $Co_2MnAl_{0.49}Si_{0.51}$, then decreases to -11.7 μV/K in Co_2MnSi. Therefore, we found that the x for the highest AHE, Seebeck effect and ANE are different in prepared CMAS films. Here we analyze the ANE in CMAS using a following linear response equation of S_{ANE},

$$\boldsymbol{S_{ANE} = \rho_{xx}\alpha_{xy} + \rho_{xy}\alpha_{xx}} \quad (4)$$

Here $\boldsymbol{\alpha_{xx}}$ and $\boldsymbol{\alpha_{xy}}$ are the longtudinal and transverse Peltier coefficient, respectively. Eq.(4) tells us that there are two different phenomenal sources in ANE. For simplifying the following explanation, we denote the first and second terms as $\boldsymbol{S_I = \rho_{xx}\alpha_{xy}}$ and $\boldsymbol{S_{II} = \rho_{xy}\alpha_{xx}}$, respectively. Since $\boldsymbol{S_{SE} = \rho_{xx}\alpha_{xx}}$, $\boldsymbol{S_{II}}$ can be converted to $\boldsymbol{S_{SE} \cdot \theta_{AHE}}$, therefore, $\boldsymbol{S_{II}}$ is regarded as the contribution of AHE on ANE induced by a Seebeck-driven longitudinal current. On the other hand, $\boldsymbol{S_I}$ originates from the direct conversion from the temperature gradient to transverse current via $\boldsymbol{\alpha_{xy}}$ as expressed in $\boldsymbol{\alpha_{xy}\nabla T = i_{xy}}$. Figure 4(c) plots $\boldsymbol{S_{II}}$ estimated from observed $\boldsymbol{S_{SE}}$ and $\boldsymbol{\theta_{AHE}}$ against x. Although we observed a large difference of x dependence between the magnitudes of AHE and ANE in the CMAS films, the trend of x dependence of $\boldsymbol{S_{II}}$ is similar to that of S_{ANE}. An important point here is that the magnitude of $\boldsymbol{S_{II}}$ is smaller than the observed S_{ANE} in whole range of x. Thus the remaining part of $\boldsymbol{S_{ANE}}$ would arise from $\boldsymbol{S_I}$ by following the eq.(4). Evaluated $\boldsymbol{S_I}$ is plotted in Figure 4(c). It can be seen that the contribution of $\boldsymbol{S_I}$ is larger than $\boldsymbol{S_{II}}$ except for Co_2MnAl. Particularly, the largest S_{ANE} of +3.6 μV/K at $x = 0.37$ arises from the constructive but dominant contribution of $\boldsymbol{S_I}$ (+2.7 μV/K) against S_{II} (+0.9 μV/K).$\boldsymbol{\alpha_{xy}}$ evaluated from $\boldsymbol{\alpha_{xy} = S_I/\rho_{xx}}$ is plotted in Fig.4(d).It is clearly appeared that $\boldsymbol{\alpha_{xy}}$ becomes larger by replacing more Al with Si,

indicating that $\boldsymbol{\alpha_{xy}}$ **is** sensitive to the position of Fermi level and atomic ordering. The $\boldsymbol{\alpha_{xy}}$ for Co_2MnAl and $Co_2MnAl_{0.63}Si_{0.37}$ films are 0.11 and 1.07A/mK, respectively. $\boldsymbol{\alpha_{xy}}$ originating from intrinsic contribution of AHE, $\boldsymbol{\alpha_{xy}^{int}}$, can be theoretically evaluated from the energy dependence of $\boldsymbol{\sigma_{xy}^{int}}$ using the following Mott's relation based on classic Boltzmann equation. [38]

$$\alpha_{xy}^{int} = \frac{1}{-eT}\int_{-\infty}^{\infty} \sigma_{xy}^{int}(\varepsilon)(\varepsilon - E_F)\left(-\frac{df}{d\varepsilon}\right)d\varepsilon \qquad (5)$$

To obtain α_{xy}^{int} at 300K, we calculated α_{xy}^{int} by setting $\pm 260meV(=0.02Ry)$ as the integration range of this calculation which is enough large for the term of $\frac{df}{d\varepsilon}(\varepsilon, T)$ to have a finite value at 300K. As shown in Fig. 4(d), calculated α_{xy}^{int} for $L2_1$ and $B2$-Co_2MnAl($Co_2MnAl_{0.63}Si_{0.37}$) are 0.92(3.08) and 0.47(0.57), respectively. Simply speaking, α_{xy}^{int} is sensitive to the shape and slope of σ_{xy}^{int} at around E_F, namely, even(odd) function-like behavior leads to small(large) α_{xy}^{int}. As we can see in Fig.3(c), $L2_1$-Co_2MnAl shows nearly even function like behavior around E_F within the integration range, whereas, $L2_1$- $Co_2MnAl_{0.63}Si_{0.37}$ shows odd function like behavior with a large negative slope, which is a reason for much larger α_{xy}^{int} in $L2_1$-$Co_2MnAl_{0.63}Si_{0.37}$. In B2 disordered case, because σ_{xy}^{int} shows very small change in both Co_2MnAl and $Co_2MnAl_{0.63}Si_{0.37}$, α_{xy}^{int} was estimated to be very small. As can be seen in Fig.4(d), experimental α_{xy} for $Co_2MnAl_{0.63}Si_{0.37}$ is close to the calculated value for $B2$-case but reasonably located in between $L2_1$ and $B2$. Therefore, we concluded that the

enlargement of α_{xy} in our CMAS thin films is attributed to not only Fermi level shifting but also the improvement of $L2_1$-atomic ordering by Si substitution for Al.

To see the effect of atomic ordering more clearly, we investigated the annealing temperature T_{ann} dependence of atomic ordering, AHE and ANE in the Co_2MnAl and $Co_2MnAl_{0.63}Si_{0.37}$ films. Figure 5(a) shows the T_{ann} dependence of the degree of $L2_1$ ordering S_{L21} evaluated by equation (3). Co_2MnAl film does not show (111) peak even after annealing at 700°C, indicating that Co_2MnAl keeps $B2$ disordered structure regardless of T_{ann}. Therefore, σ_{xy} in Co_2MnAl film is around 300S/cm and shows no remarkable variation against T_{ann} (Fig.5(b)). In contrast, tiny (111) that appears at T_{ann} = 600°C in $Co_2MnAl_{0.63}Si_{0.37}$ was strongly enlarged by increasing T_{ann}, up to 650°C. S_{L21} increases from 0.32 at 600°C to 0.66 at 650°C. Oppositely, (111) peak does not appears at 500 °C . Observed σ_{xy} in $Co_2MnAl_{0.63}Si_{0.37}$ gradually increases with T_{ann} (Fig.5(b)) from 136 S/cm at 500°C to 275 S/cm at 700°C , whose tendency is in qualitative agreement with the calculated σ_{xy}^{int} shown in Fig.3(d). A drastic increase of S_{SE} and S_{ANE} were also observed in the $Co_2MnAl_{0.63}Si_{0.37}$ annealed at above 650°C(Fig.5(c)-(e)) in contrast to no remarkable change of them in the Co_2MnAl against T_{ann}, indicating that the enlargement of both S_{SE} and S_{ANE} arises from the improvement of $L2_1$-ordering. The highest S_{ANE}[7,8] of 5.7 μV/K, which is comparable to the previous reports in Co_2MnGa[7,8], was observed for the $Co_2MnAl_{0.63}Si_{0.37}$ film annealed at 650°C. At the same time, as can be seen in Fig.5(f), α_{xy} reaches 1.68A/mK at 650°C which is located in between theoretical α_{xy}^{int} for $L2_1$ and $B2$ as expected from the evaluated imperfect S_{L21}. Such large α_{xy} gives rise to dominant S_I contribution of 4.0 μV/K for the total ANE of

294 5.7μV/K. Therefore, it is suggested that giant ANE in CMAS film achieved in this
295 study is due to both the Fermi level shifting and improvement of $L2_1$-atomic ordering in
296 Co_2MnAl which has been predicted as a Weyl semi-metal. We should note that because
297 our CMAS films do not have ideal $L2_1$-ordering, higher ANE might be possible by
298 improving the degree of $L2_1$-ordering.
299
300
301 In conclusion, in this work, we studied anomalous Hall and Nernst effect in the
302 $Co_2MnAl_{1-x}Si_x$ from both experiment and first-principle calculation to see the effect of
303 Fermi level position and the degree of atomic ordering on AHE and ANE. It was clearly
304 confirmed that Fermi level shifts toward higher energy and $L2_1$-ordering improves with
305 increasing Si composition ratio x. Observed σ_{xy} in the Co_2MnAl film having no
306 $L2_1$-ordering is much smaller than the calculated intrinsic σ_{xy} for $L2_1$-orderd structure
307 but close to our calculation for B2-disordered structure, suggesting that theoretically
308 predicted large AHE due to the existence of Weyl points in Co_2MnAl is weaken by
309 unavoidable B2 disordering in reality. Although Al substitution with Si does not
310 strongly affect σ_{xy}, the transverse Peltier coefficient α_{xy} was clearly enlarged with
311 increasing Si, and the highest α_{xy} was obtained in $Co_2MnAl_{0.63}Si_{0.37}$. As predicted by
312 our calculation, α_{xy} was enlarged by improving $L2_1$-ordering in $Co_2MnAl_{0.63}Si_{0.37,}$ and
313 finally giant thermopower of ANE of 5.7μV/K was achieved in $Co_2MnAl_{0.63}Si_{0.37}$ film
314 having the mixture of $L2_1$- and $B2$-phase. Our result indicates that, both Fermi level
315 tuning and high atomic ordering is critically important to realize exotic transverse

316 transports in Co-based Heusler Weyl semi-metals. This knowledge will be beneficial for
317 a future material development to realize practical thermoelectric applications using
318 ANE.
319
320
321
322
323
324
325
326
327
328
329
330
331
332
333
334
335
336
337

[1] Y. Sakuraba, K. Hasegawa, M. Mizuguchi, T. Kubota, S. Mizukami, T. Miyazaki, and K. Takanashi, Appl. Phys. Express **6**, 033003 (2013).
[2] Y. Sakuraba, Scr. Mater. **111**, 29 (2016).
[3] Z. Weinan and Y. Sakuraba, Appl. Phys. Express (2020).
[4] M. Ikhlas, T. Tomita, T. Koretsune, M.-T. Suzuki, D. Nishio-Hamane, R. Arita, Y. Otani, and S. Nakatsuji, Nat. Phys. **13**, 1085 (2017).
[5] K. Hasegawa, M. Mizuguchi, Y. Sakuraba, T. Kamada, T. Kojima, T. Kubota, S. Mizukami, T. Miyazaki, and K. Takanashi, Appl. Phys. Lett. **106**, 252405 (2015).
[6] G. Chang, S.-Y. Xu, X. Zhou, S.-M. Huang, B. Singh, B. Wang, I. Belopolski, J. Yin, S. Zhang, A. Bansil, H. Lin, and M. Zahid Hasan, Phys. Rev. Lett. **119**, 156401 (2017).
[7] A. Sakai, Y.P. Mizuta, A. Agung Nugroho, R. Sihombing, T. Koretsune, M.-T. Suzuki, N. Takemori, R. Ishii, D. Nishio-Hamane, R. Arita, P. Goswami, and S. Nakatsuji, Nat. Phys. **14**, 1119 (2018).
[8] S.N. Guin, K. Manna, J. Noky, S.J. Watzman, C. Fu, N. Kumar, W. Schnelle, C. Shekhar, Y. Sun, J. Gooth, and C. Felser, NPG Asia Mater. **11**, (2019).
[9] I. Belopolski, K. Manna, D.S. Sanchez, G. Chang, B. Ernst, J. Yin, S.S. Zhang, T. Cochran, N. Shumiya, H. Zheng, B. Singh, G. Bian, D. Multer, M. Litskevich, X. Zhou, S.M. Huang, B. Wang, T.R. Chang, S.Y. Xu, A. Bansil, C. Felser, H. Lin, and M. Zahid Hasan, Science (80-.). **365**, 1278 (2019).
[10] K.I. Uchida, T. Kikkawa, T. Seki, T. Oyake, J. Shiomi, Z. Qiu, K. Takanashi, and E. Saitoh, Phys. Rev. B **92**, 094414 (2015).
[11] Y.P. Mizuta and F. Ishii, Sci. Rep. **6**, 28076 (2016).
[12] D.J. Kim, K.D. Lee, S. Surabhi, S.G. Yoon, J.R. Jeong, and B.G. Park, Adv. Funct. Mater. **26**, 5507 (2016).
[13] H. Narita, M. Ikhlas, M. Kimata, A.A. Nugroho, S. Nakatsuji, and Y. Otani, Appl. Phys. Lett. **111**, 202404 (2017).
[14] S. Tu, J. Hu, G. Yu, H. Yu, C. Liu, F. Heimbach, X. Wang, J. Zhang, Y. Zhang, A. Hamzić, K.L. Wang, W. Zhao, and J.-P. Ansermet, Cit. Appl. Phys. Lett **111**, 222401

(2017).
[15] T.C. Chuang, P.L. Su, P.H. Wu, and S.Y. Huang, Phys. Rev. B **96**, 174406 (2017).
[16] Z. Yang, E.A. Codecido, J. Marquez, Y. Zheng, J.P. Heremans, and R.C. Myers, AIP Adv. **7**, 095017 (2017).
[17] S. Isogami, K. Takanashi, and M. Mizuguchi, Appl. Phys. Express **10**, 073005 (2017).
[18] T. Miyasato, N. Abe, T. Fujii, A. Asamitsu, S. Onoda, Y. Onose, N. Nagaosa, and Y. Tokura, Phys. Rev. Lett. **99**, 086602 (2007).
[19] J. Kübler and C. Felser, Phys. Rev. B - Condens. Matter Mater. Phys. **85**, 012405 (2012).
[20] J.C. Tung and G.Y. Guo, New J. Phys. **15**, 033014 (2013).
[21] J. Kübler and C. Felser, EPL **114**, 47005 (2016).
[22] E. Vilanova Vidal, G. Stryganyuk, H. Schneider, C. Felser, and G. Jakob, Appl. Phys. Lett. **99**, 132509 (2011).
[23] Y. Yao, L. Kleinman, a H. MacDonald, J. Sinova, T. Jungwirth, D. Wang, E. Wang, and Q. Niu, Phys. Rev. Lett. **92**, 037204 (2004).
[24] N. Nagaosa, J. Sinova, S. Onoda, A.H. MacDonald, and N.P. Ong, Rev. Mod. Phys. **82**, 1539 (2010).
[25] Y. Sakuraba, J. Nakata, M. Oogane, H. Kubota, Y. Ando, A. Sakuma, and T. Miyazaki, Japanese J. Appl. Physics, Part 1 Regul. Pap. Short Notes Rev. Pap. **44**, 6535 (2005).
[26] T. Nakatani, S. Li, Y. Sakuraba, T. Furubayashi, and K. Hono, IEEE Trans. Magn. **2**, 54 (2017).
[27] R.Y. Umetsu, K. Kobayashi, A. Fujita, R. Kainuma, and K. Ishida, Scr. Mater. **58**, 723 (2008).
[28] Y. Sakuraba, K. Takanashi, Y. Kota, T. Kubota, M. Oogane, A. Sakuma, and Y. Ando, Phys. Rev. B **81**, 144422 (2010).
[29] Y. Sakuraba, S. Kokado, Y. Hirayama, T. Furubayashi, H. Sukegawa, S. Li, Y.K. Takahashi, and K. Hono, Appl. Phys. Lett. **104**, 172407 (2014).
[30] See Supplemental Material at (URL) for the detail of the evaluation method of ∇T using the on-chip thermometer.
[31] I. Turek, *Electronic Structure of Disordered Alloys, Surfaces and Interfaces, 1997th Ed. (Springer, Berlin, 1996)*. (1996).

[32] I. Turek, J. Kudrnovsk, and V. Drchal, Phys. Rev. B **89**, 064405 (2014).
[33] F.J. Yang, Y. Sakuraba, S. Kokado, Y. Kota, A. Sakuma, and K. Takanashi, Phys. Rev. B **86**, 020409(R) (2012).
[34] S. Kokado, M. Tsunoda, K. Harigaya, and A. Sakuma, J. Phys. Soc. Japan **81**, 24705 (2012).
[35] See Supplemental Material at (URL) for the detail of the CMAS composition dependence of AMR ratio.
[36] J.C. Prestigiacomo, D.P. Young, P.W. Adams, and S. Stadler, Cit. J. Appl. Phys. **115**, 242408 (2014).
[37] S. Sangiao, L. Morellon, G. Simon, J.M. De Teresa, J.A. Pardo, J. Arbiol, and M.R. Ibarra, Phys. Rev. B - Condens. Matter Mater. Phys. **79**, 2 (2009).
[38] N.F. Mott and H. Jones, in *Clarendon Press. Oxford* (1936), pp. 308–314.

Acknowledgements

Authors thank K. Masuda, K. Sumida, A. Kimura, W. Zhou, K. Takanashi, S. Maekawa, K. Hono, and K. Uchida for valuable discussions and N. Kojima, H. Ikeda, B. Masaoka for a technical support. This work was supported by a JSPS KAKENHI Grant-in-Aid for Young Scientists (A) (No. JP2670945), PRESTO from the Japan Science and Technology Agency (No. JPMJPR17R5) and NEDO.

Figure 1 (a),(b) The schematic views of $L2_1$- and $B2$ structure of CMAS. (c) Out-of-plane XRD patterns for $Co_2MnAl_{1-x}Si_x$ thin films annealed at 600°C. The peaks denoted by * originate from MgO (001) substrate. The inset shows Si composition x dependence of lattice constant a evaluated from position of (004) peak position. (d)XRD patterns measured by tilting the film normal plane by 54.7°to see (111) superlattice peak. (e),(f) The x dependence of $I_{002}^{obs}/I_{004}^{obs}$, $I_{111}^{obs}/I_{004}^{obs}$, S_{B2} and S_{L21} evaluated by equation (2) and (3), respectively.

Figure 2 (a) Perpendicular magnetic field H dependence of anomalous Hall resistivity ρ_{xy} for $Co_2MnAl_{1-x}Si_x$ thin films measured at 300 K. Si composition dependence of ρ_{xx} (b), ρ_{yx} (c), anomalous Hall angle $|\theta_{AHE}|$ (c) and σ_{xy} (c). The data measured at 10 and 300K are shown in (b)-(e). Theoretical σ_{xy}^{int} for $L2_1$-and $B2$- Co_2MnAl and $Co_2MnAl_{0.67}Si_{0.33}$ are also plotted in (e).

Figure 3 First principles calculation of the spin-resolved DOS for Co_2MnAl(a) and $Co_2MnAl_{0.67}Si_{0.33}$(b). For both compositions we calculated the DOS in $L2_1$ and $B2$ disordered structure. (b) Calculated energy dependence of σ_{xy} for B2 and $L2_1$-ordered Co_2MnAl(c) and $Co_2MnAl_{0.63}Si_{0.37}$(d).

Figure 4 Si composition x dependence of S_{ANE} (a), S_{SE} (b), S_I and S_I (c) and α_{xy}(d). The inset of (b) shows the external magnetic field dependence of V_{ANE} normalized by the sample width w and given temperature gradient ∇T in CMAS films. Theoretically calculated α_{xy}^{int} using eq.(3) are also plotted in (d)

Figure 5 (a) T_{ann} dependence of S_{L21} in Co_2MnAl and $Co_2MnAl_{0.63}Si_{0.37}$ films. Inset shows XRD patterns in Co_2MnAl and $Co_2MnAl_{0.63}Si_{0.37}$ thin films in the 2θ range of (111) peak. T_{ann} dependence of σ_{xy}, S_{SE}, S_{ANE} and α_{xy} in Co_2MnAl and $Co_2MnAl_{0.63}Si_{0.37}$ are shown in (b),(c), (e) and (f), respectively. The arrows in (f) is the theoretical α_{xy}^{int} for $L2_1$ and $B2$ $Co_2MnAl_{0.63}Si_{0.37}$. (d)External magnetic field

dependence of V_{ANE} normalized by the sample width w and given temperature gradient ∇T in $Co_2MnAl_{0.63}Si_{0.37}$ annealed at different temperature.

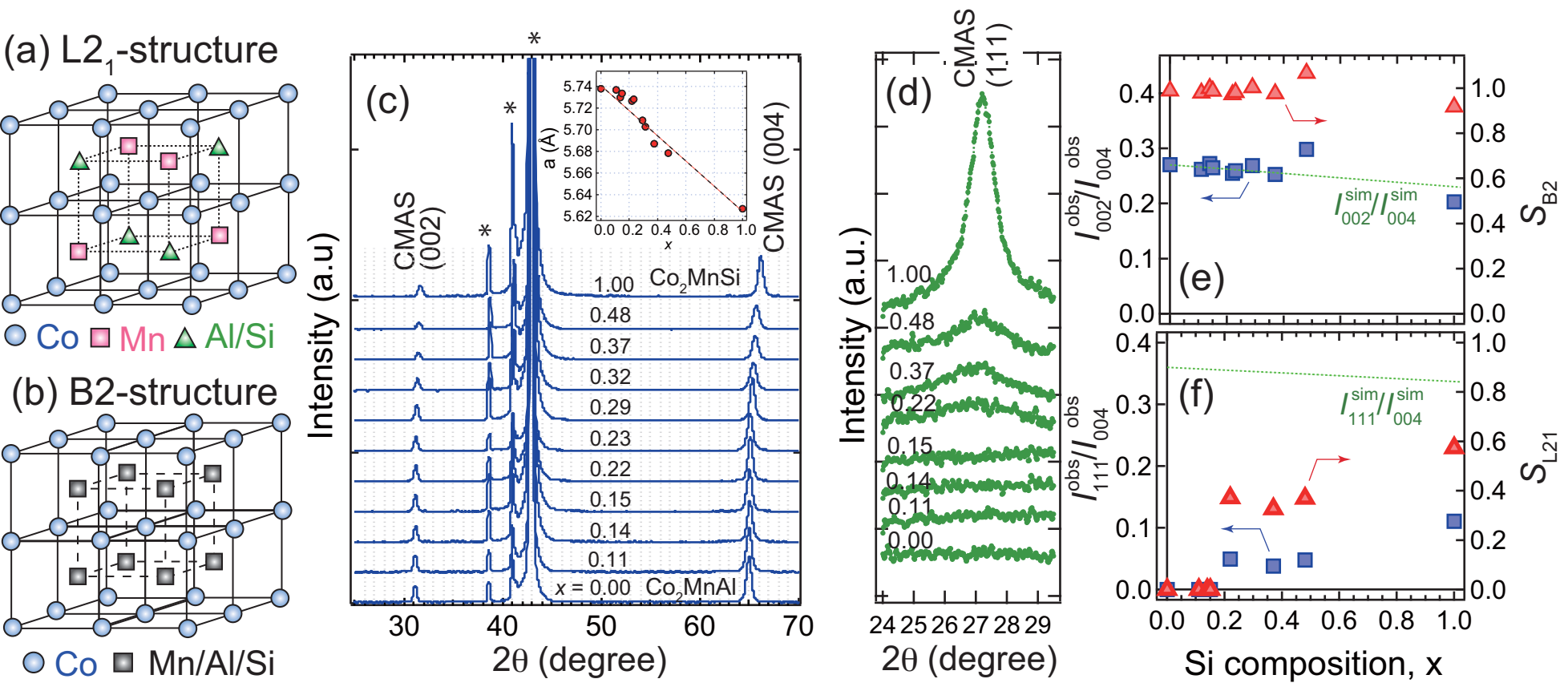
(a) L2$_1$-structure
Co
Mn
Al/Si
(b) B2-structure
Co
Mn/Al/Si
(c)
CMAS (002)
CMAS (004)
*
a (Å)
x
1.00 Co$_2$MnSi
0.48
0.37
0.32
0.29
0.23
0.22
0.15
0.14
0.11
x = 0.00 Co$_2$MnAl
Intensity (a.u)
2θ (degree)
(d)
CMAS (111)
Intensity (a.u.)
2θ (degree)
(e)
$I^{obs}_{002}/I^{obs}_{004}$
$I^{sim}_{002}/I^{sim}_{004}$
S_{B2}
(f)
$I^{obs}_{111}/I^{obs}_{004}$
$I^{sim}_{111}/I^{sim}_{004}$
S_{L21}
Si composition, x

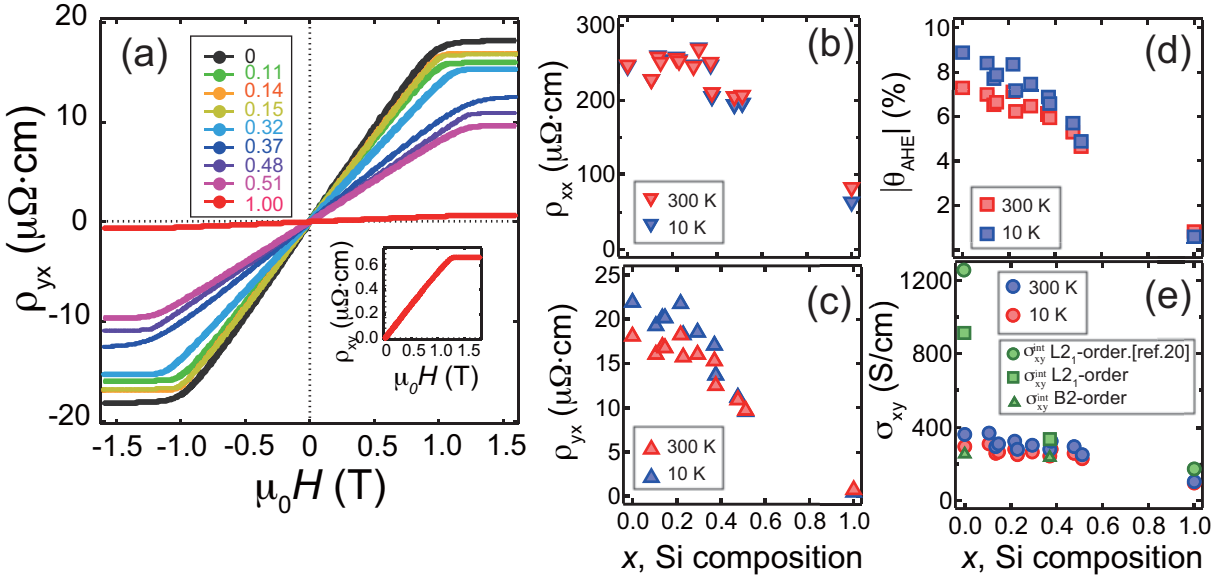

Si composition

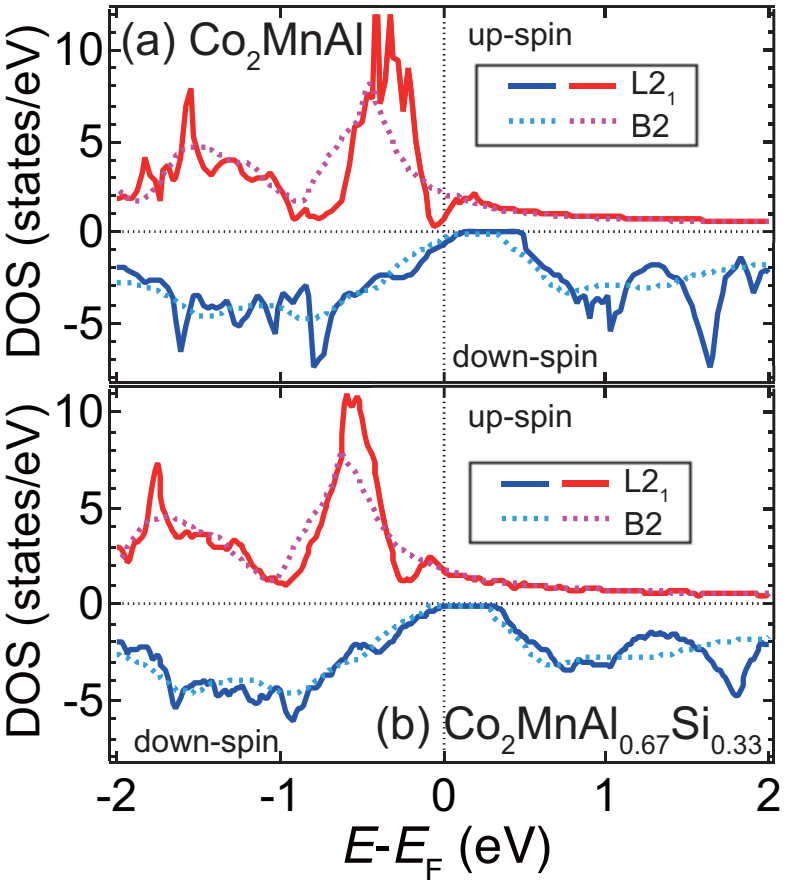
(a) Co2MnAl
up-spin
L21
B2
down-spin
DOS (states/eV)
10
5
0
-5
(b) Co2MnAl0.67Si0.33
up-spin
L21
B2
down-spin
DOS (states/eV)
10
5
0
-5
-2
-1
0
1
2
E-EF (eV)

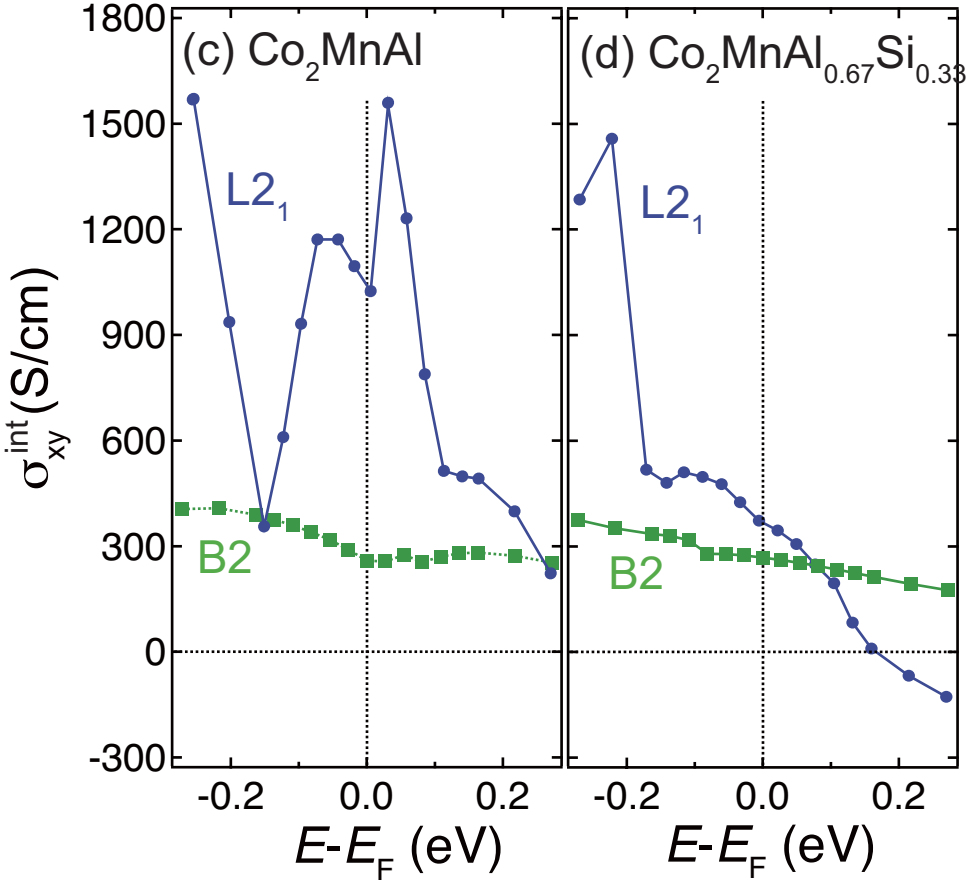
(c) Co2MnAl
(d) Co2MnAl0.67Si0.33
σxyint(S/cm)
1800
1500
1200
900
600
300
0
-300
L21
B2
L21
B2
-0.2
0.0
0.2
-0.2
0.0
0.2
E-EF (eV)
E-EF (eV)

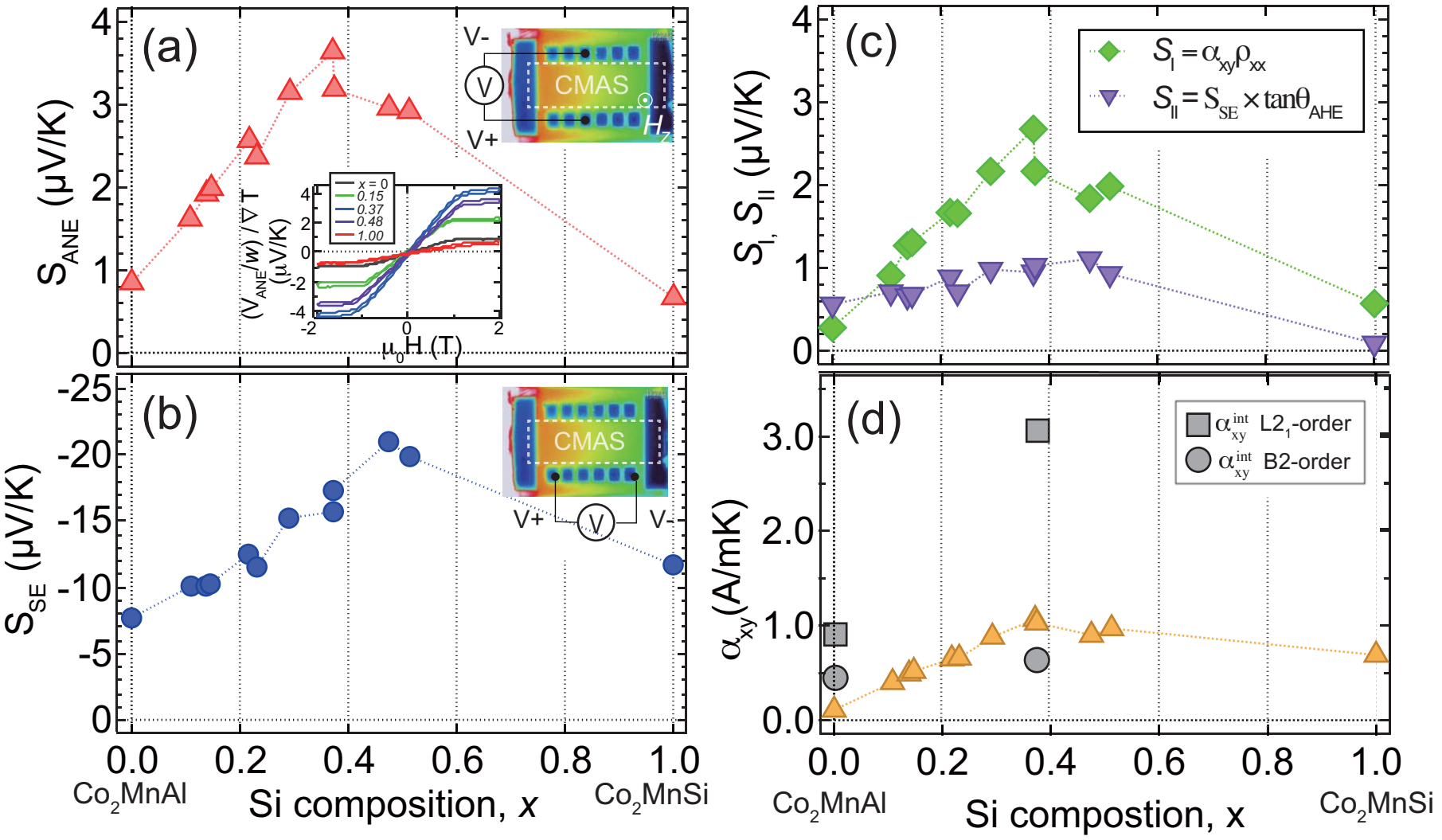
(a)
S_{ANE} (μV/K)
V-
V
V+
CMAS
H_z
$(V_{ANE}/w)/\nabla T$ (μV/K)
x = 0
0.15
0.37
0.48
1.00
$\mu_0 H$ (T)
(b)
S_{SE} (μV/K)
CMAS
V+
V
V-
(c)
$S_{\perp}, S_{\parallel}$ (μV/K)
$S_{\perp} = \alpha_{xy}\rho_{xx}$
$S_{\parallel} = S_{SE} \times \tan\theta_{AHE}$
(d)
α_{xy} (A/mK)
α_{xy}^{int} $L2_1$-order
α_{xy}^{int} B2-order
Co_2MnAl
Si composition, x
Co_2MnSi
Co_2MnAl
Si compostion, x
Co_2MnSi

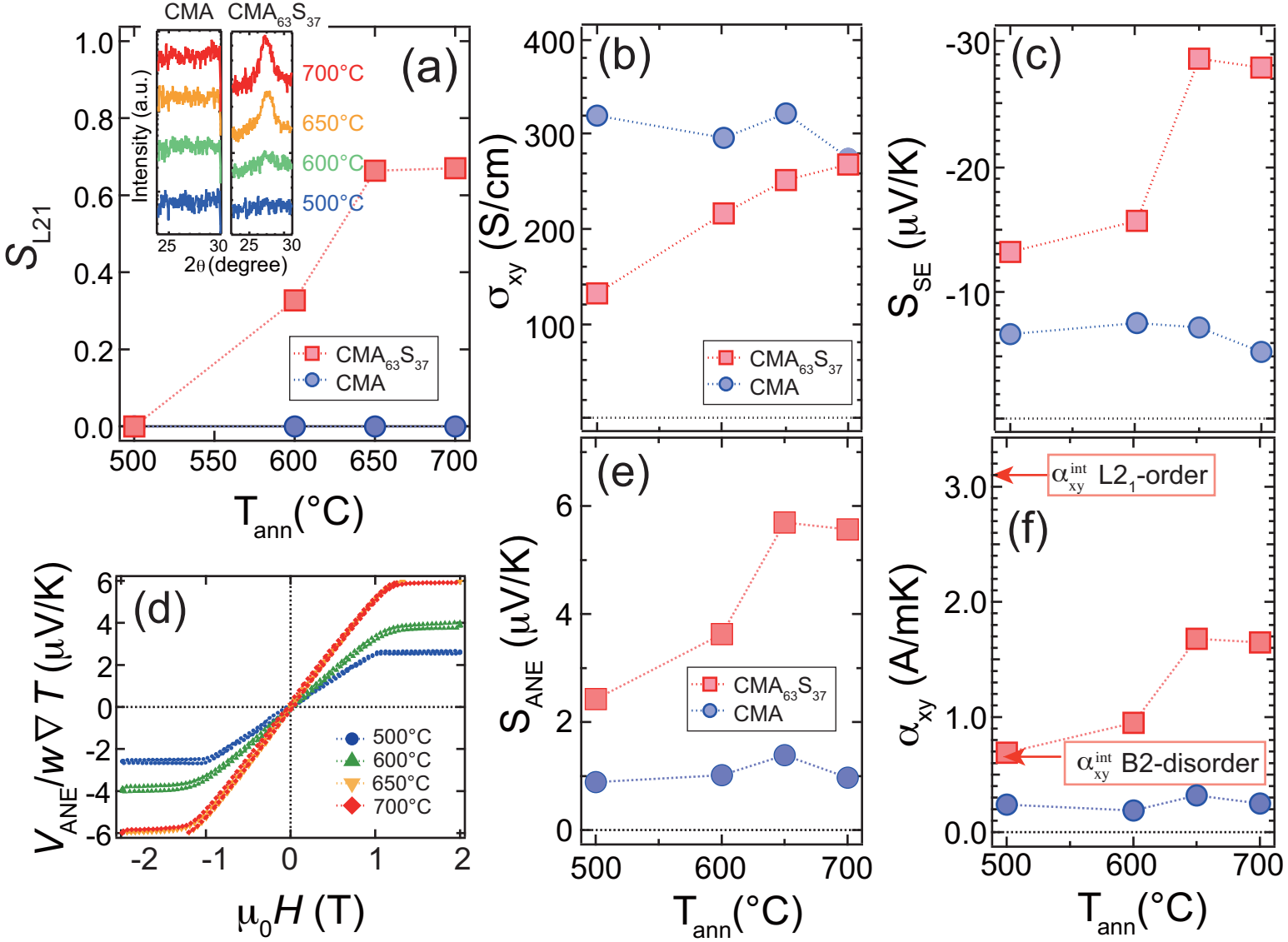
(a)
CMA
CMA63S37
Intensity (a.u.)
700°C
650°C
600°C
500°C
2θ (degree)
S_L21
T_ann (°C)
(b)
σ_xy (S/cm)
(c)
S_SE (μV/K)
(d)
V_ANE/wΔT (μV/K)
μ0H (T)
(e)
S_ANE (μV/K)
(f)
α_xy (A/mK)
α_xy^int L21-order
α_xy^int B2-disorder

Tann